JACS
JOURNAL OF THE AMERICAN CHEMICAL SOCIETY
pubs.acs.org/JACS
Article

Superior Charge Transport in Ni-Diamine Conductive MOFs

Jiande Wang,[§] Tianyang Chen,[§] Mingyu Jeon, Julius J. Oppenheim, Bowen Tan, Jihan Kim, and Mircea Dincă*

Cite This: J. Am. Chem. Soc. 2024, 146, 20500−20507
Read Online
ACCESS | Metrics & More | Article Recommendations | Supporting Information

ABSTRACT: Two-dimensional conductive metal−organic frameworks (2D cMOFs) are an emerging class of crystalline van der Waals layered materials with tunable porosity and high electrical conductivity. They have been used in a variety of applications, such as energy storage and conversion, chemiresistive sensing, and quantum information. Although designing new conductive 2D cMOFs and studying their composition/structure−property relationships have attracted significant attention, there are still very few examples of 2D cMOFs that exhibit room-temperature electrical conductivity above 1 S cm^{-1}, the value exhibited by activated carbon, a well-known porous and conductive material that serves in myriad applications. When such high conductivities are achieved, Ni-diamine linkages are often involved, yet Ni-diamine MOFs remain difficult to access. Here, we report two new 2D cMOFs made through ortho-diamine connections: $M_3(HITT)_2$ (M = Ni, Cu; HITT = 2,3,7,8,12,13-hexaiminotetraazanaphthotetraphene). The electrical conductivity of $Ni_3(HITT)_2$ reaches 4.5 S cm^{-1} at 298 K, whereas the conductivity of $Cu_3(HITT)_2$ spans from 0.05 ($2Cu^+Cu^{2+}$) to 10^{-6} ($3Cu^{2+}$) upon air oxidation, much lower than that of $Ni_3(HITT)_2$. Spectroscopic analysis reveals that $Ni_3(HITT)_2$ exhibits significantly stronger in-plane π-d conjugation and higher density of charge carriers compared to $Cu_3(HITT)_2$, accounting for the higher electrical conductivity of $Ni_3(HITT)_2$. Cu^{2+}/Cu^+ mixed valency modulates the energy level and carrier density of $Cu_3(HITT)_2$, allowing for a variation of electrical conductivity over 4 orders of magnitude. This work provides a deeper understanding of the influence of metal nodes on electrical conductivity and confirms ortho-diamine linkers as privileged among ligands for 2D cMOFs.

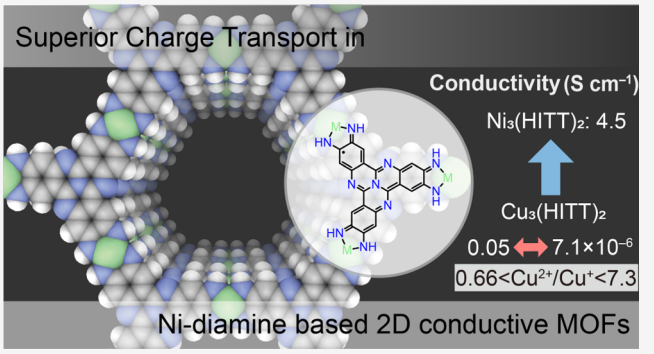

INTRODUCTION

Although the vast majority of metal−organic frameworks (MOFs) are electrical insulators, the past decade has witnessed the emergence of electrically conducting MOFs (cMOFs),[1,2] which exhibit semiconducting, metallic, or superconducting behaviors with conductivities exceeding 1000 S cm^{-1}.[3−6] They have demonstrated promising performance in various applications including but not limited to electrocatalysis,[7,8] field-effect transistors,[9] chemiresistive sensors,[10−14] energy storage,[15−20] and quantum information.[21] Two-dimensional (2D) layered MOFs, which feature in-plane extended π-d conjugation between ligands and metals and out-of-plane π−π stacking of 2D sheets, have shown the highest electrical conductivities among cMOFs. Understanding the origin of their high electrical conductivities is crucial for future material design and optimization of their performance in the aforementioned applications. Empirically, 2D cMOFs based on phenylenediamine ligands generally show higher electrical conductivity than their catechol analogues. Among diamine-based MOFs, the Ni-diamine combination has given rise to particularly conductive materials, as seen for instance in the series $M_3(HITP)_2$ (HITP = 2,3,6,7,10,11-hexaiminotriphenylene; M = Ni, Cu, Co), where the nature of the metal ion exerts enormous influence on electrical conductivity.[22] One decade after its discovery, $Ni_3(HITP)_2$ still figures as one of the most conductive 2D cMOFs among dozens of other materials reported since then.[23] However, designing and isolating new Ni-diamine MOFs has proven difficult, as polyaromatic ligands with multiple phenylenediamine groups become extremely electron-rich and thus difficult to isolate, handle, and incorporate into crystalline materials.[24]

Indeed, despite the now large and growing number of 2D cMOFs, well-characterized diamine-based materials have been reported with only five ligands: HAB, HATP, $MPc(NH)_8$, HAR_3-TAT and HATBim (Figure 1).[5,22,25−27] Furthermore, only HAB- and HATP-based 2D cMOFs can exhibit conductivity higher than that of activated carbons (ca. 1 S cm^{-1}), an important class of porous and conductive materials which have poor structural tunability and pore-size control.

Received: May 21, 2024
Revised: June 29, 2024
Accepted: July 8, 2024
Published: July 15, 2024

https://doi.org/10.1021/jacs.4c06935
J. Am. Chem. Soc. 2024, 146, 20500−20507

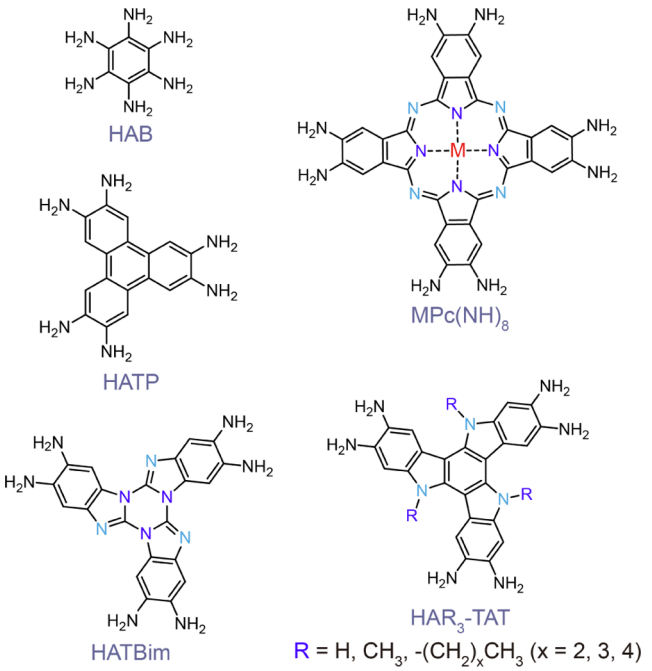

Figure 1. Reported diamine-based ligands for 2D cMOFs.

Although the other heteroatom-containing ligands (MPc-$(NH)_8$, HAR_3-TAT and HATBim) provide abundant active sites for postsynthetic modulation, they often yield 2D cMOFs with moderate conductivity of 0.1 S cm^{-1} or less. Therefore, there is a significant need for developing new diamine-based 2D cMOFs that exhibit conductivities higher than 1 S cm^{-1} while possessing capabilities for facile postsynthetic modification. Perhaps even more importantly, understanding the influence of metal centers, including their identity and valence, on the electrical conductivity of diamine-based 2D cMOFs is crucial for iterative material design.

Here, we report the design, synthesis, and characterization of $M_3(HITT)_2$ (M = Ni, Cu; HITT = 2,3,7,8,12,13-hexaiminotetraazanaphthotetraphene) based on the ligand HATT (2,3,7,8,12,13-hexaaminotetraazanaphthotetraphene). The heterocyclic core in HATT, with its expanded π-conjugated plane compared to the more common triphenylene or benzene core in other diamine ligands allows more efficient interligand interactions and more organized π-stacking, as observed in similar π systems. Furthermore, the presence of three peripheral electron-withdrawing pyridinic nitrogen atoms in HATT significantly reduces its electron density, leading to a lower energy of its lowest unoccupied molecular orbital (LUMO), −0.82 eV, compared to that of 2,3,6,7,10,11-hexaaminotriphenylene (HATP), 0.41 eV (Figure S1). Similarly, HATT has a significantly lower highest occupied molecular orbital−lowest unoccupied molecular orbital (HOMO−LUMO) gap of 3.39 eV relative to 4.20 eV for HATP. This HOMO−LUMO gap is also slightly lower than the gap of 3.43 eV for the catechol analogue, 2,3,7,8,12,13-hexahydroxy tetraazanaphthotetraphene (HHTT) (Figure S1). Notably, these ligand design features already proved critical in allowing HHTT to form single crystals of 2D cMOFs with high electrical conductivity.[28] As such, we surmised that HATT could lead to materials with even higher conductivity than the catechol analog, as enabled by favorable $\pi-\pi$ interactions and more covalent bonding between metal and amino groups.

RESULTS AND DISCUSSION

Reaction of $Ni(NO_3)_2{\cdot}6H_2O$ and HATT·3HCl (see synthetic details in Supporting Information and Figures S2−S10) in a mixture of *N*,*N*-dimethylformamide (DMF) and H_2O under

Scheme 1. Synthetic Scheme for Accessing $M_3(HITT)_2$

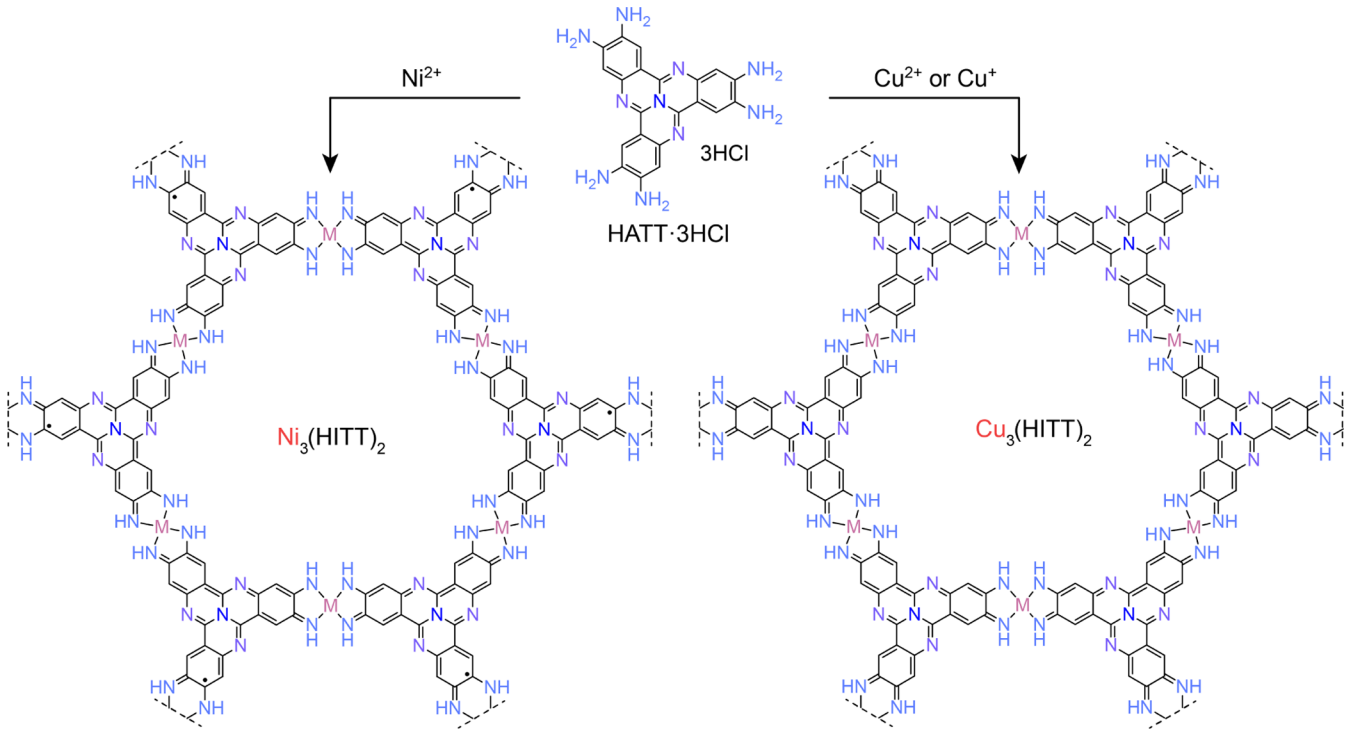

https://doi.org/10.1021/jacs.4c06935
J. Am. Chem. Soc. 2024, 146, 20500−20507

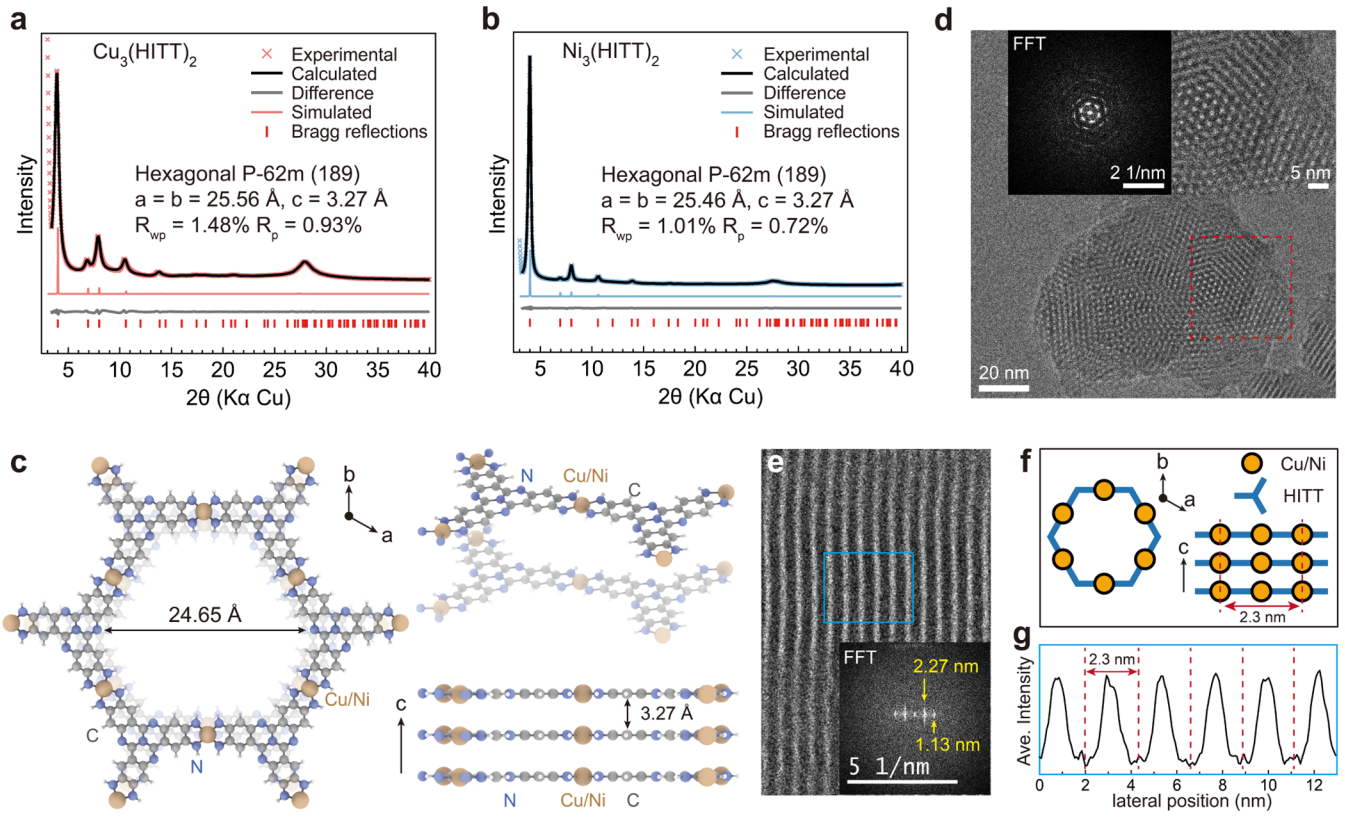

Figure 2. Experimental, Pawley refined, and simulated PXRD patterns for (a) $Cu_3(HITT)_2$, and (b) $Ni_3(HITT)_2$. (c) The modeled crystal structure along the *c* direction and parallel to the *ab* plane. Gray, blue and brown spheres represent C, N, and Cu/Ni atoms, respectively; Cryo-HRTEM image of (d) $Cu_3(HITT)_2$ and (e) $Ni_3(HITT)_2$ (inset: FFT). (f) Schematic of $Ni_3(HITT)_2$ and $Cu_3(HITT)_2$ structure illustrated for three layers in an eclipsed stacking for imaging perpendicular and parallel to the 2D layers. (g) Average intensity from the blue box in the HRTEM image.

air at 45 °C deprotonates and oxidizes HATT, yielding $Ni_3(HITT)_2$ (Scheme 1) as a black powder consisting of irregularly shaped particles measuring between 100 and 200 nm, as determined by scanning electron microscopy (SEM, Figure S11). Synthesis of $Ni_3(HITT)_2$ at lower temperature does not form solid products, whereas increased temperature leads to lower crystallinity (Figure S12). Interestingly, unlike the synthesis of most copper-based 2D cMOFs,[5,18,22,28] the reaction between HATT·3HCl and Cu^{2+} salts (e.g., $Cu(NO_3)_2$ and $CuCl_2$) produces only poorly crystalline $Cu_3(HITT)_2$ powders (Figures S13 and S14). Better results are instead obtained with Cu^+ precursors, such as CuCl and CuI, which lead to the formation of well-defined $Cu_3(HITT)_2$ nanorods with significantly improved crystallinity (Figures S14 and S15). Previous studies have shown that solvated Cu^{2+} ions react extremely rapidly with phenylenediamine-based linkers to produce poorly crystalline samples,[12] and that optimizing solvent systems to limit the solubility of the Cu^{2+} precursor can improve the crystallinity of the corresponding 2D cMOFs.[22] In our case, the low solubility of Cu^+ salts likely slows down the MOF nucleation process, leading to better quality $Cu_3(HITT)_2$. In line with retarded nucleation and growth rates, synthesizing $Cu_3(HITT)_2$ at 0 °C leads to significantly better crystallinity relative to samples produced at 25 or 65 °C (Figure S13).

Pawley refinements of the powder X-ray diffraction (PXRD) data (Figure 2a,b) provided best fits for both materials in the hexagonal space group $P\bar{6}2m$. Therefore, $Ni_3(HITT)_2$ and $Cu_3(HITT)_2$ are isostructural, with only slightly different lattice parameters of $a = b = 25.56$ and $c = 3.27$ Å for $Cu_3(HITT)_2$, and $a = b = 25.46$ and $c = 3.27$ Å for $Ni_3(HITT)_2$. These data point to both materials forming 2D sheets with fully eclipsed stacking (AA stacking, Figure 2c), similar to the corresponding catechol materials M_3HHTT_2 (M = Cu, Ni).[28] High resolution cryogenic transmission electron microscopy (cryo-TEM) further confirmed the structural details obtained from diffraction analysis, with both materials exhibiting hexagonal lattices (Figures 2d,g, S16 and S17). Imaging perpendicular to the *z*-axis (Figure 2e) reveals contrast fringes that run approximately parallel to the direction normal to the 2D sheets. The fast Fourier transform (FFT) shows a fringe periodicity of 2.3 nm (Figure 2g, red arrows), similar to the unit cell parameter. Further inspection indicates an additional periodic $\pi-\pi$ feature with a spacing of 0.33 nm for both $Ni_3(HITT)_2$ and $Cu_3(HITT)_2$ (Figures S16 and S17), itself in good agreement with the Pawley refinement for the *c* unit cell parameter. All of the high resolution cryo-EM data suggests that the 2D layers stack in an eclipsed configuration, as illustrated in Figure 2f.

Thermogravimetric analysis (TGA) of $M_3(HITT)_2$ showed guest solvent molecules are likely eliminated before reaching ~80 °C. $Ni_3(HITT)_2$ exhibits subsequent significant weight loss above 300 °C, whereas $Cu_3(HITT)_2$ loses significant mass at much lower temperature starting at 200 °C (Figure S18). Notably, PXRD patterns of $Cu_3(HITT)_2$ at variable temperature reveal a clear decrease of crystallinity starting even at 90 °C, whereas $Ni_3(HITT)_2$ retains its crystallinity until at least 150 °C (Figures S19 and S20). N_2 adsorption isotherms

https://doi.org/10.1021/jacs.4c06935
J. Am. Chem. Soc. 2024, 146, 20500−20507

measured at 77 K reveal that both materials are permanently microporous, with Brunauer–Emmett–Teller (BET) apparent surface areas of 895.9 $m^2 g^{-1}$ for $Ni_3(HITT)_2$ and 767.5 $m^2 g^{-1}$ for $Cu_3(HITT)_2$ (Figures S21 and S22). These values are on par with those of other 2D cMOFs.[28] Fitting the N_2 absorption isotherms to Barrett–Joyner–Halenda (BJH) model revealed pore size distributions centered at 1.8 nm for both materials, matching well with their model structures (Figures S23 and S24).[29]

High-resolution X-ray photoelectron spectra (XPS) of $M_3(HITT)_2$ indicate the presence of only Ni^{2+} in $Ni_3(HITT)_2$, as verified by the Ni $2p_{3/2}$ binding energy (BE) of 856 eV, whereas the presence of two Cu 2p peaks at BEs of 934.1 and 932.5 eV indicates Cu^{2+}/Cu^+ mixed valency for $Cu_3(HITT)_2$ (Figures S25–S27). The deconvolution of the Cu $2p_{3/2}$ spectrum revealed a ratio of Cu^{2+}/Cu^+ of 0.66 regardless of the valence of the Cu precursor salts. This corresponds to a formula unit with ~1.2 Cu^{2+} and ~1.8 Cu^+ ions for $Cu_3(HITT)_2$ (Figures S26 and S27, see Supporting Information for the details of deconvolution and quantification of Cu^{2+} and Cu^+). Correspondingly, we advance that the HITT ligands are triply oxidized and 6-fold deprotonated in $Ni_3(HITT)_2$ (i.e., they are best described as $HITT^{3-}$), whereas HITT ligands are also 6-fold deprotonated but quadruply oxidized in $Cu_3(HITT)_2$, which is best described as $(Cu^+)_2(Cu^{2+})(HITT^{2-})_2$ (Schemes 1 and S1).

The bulk electrical conductivities of $M_3(HITT)_2$ were determined by four-contact probe measurements of pressed polycrystalline pellets (see Methods for measurement details; Figure S28). $Ni_3(HITT)_2$ exhibits a conductivity of up to 4.5 S cm^{-1} ($\sigma_{average}$ = 3.45 S cm^{-1}) at 298 K (Figure S29), situating it in the upper echelon even for 2D cMOFs (Table S1). In contrast, $Cu_3(HITT)_2$ shows a lower conductivity of 0.05 S cm^{-1} ($\sigma_{average}$ = 0.029 S cm^{-1}) (Figures 3 and S29), as commonly observed for Cu-based materials across metal-diamine MOFs.

Variable-temperature (VT) conductivity measurements (see Methods for measurement details) reveal that both materials show thermally activated transport. Fitting the VT conductivity data to an Arrhenius model:

$$\sigma_{e,T} = \sigma_{e,\infty} \exp\left(-\frac{E_A}{k_B T}\right)$$

where $\sigma_{e,\infty}$ is the temperature-independent prefactor, E_A is the activation energy, k_B is the Boltzmann constant, and T is the absolute temperature, gives a linear relationship with $1/T$ between 300 and 200 K, yielding E_A of 163 and 43 meV for $Cu_3(HITT)_2$ and $Ni_3(HITT)_2$, respectively (Figure 3a). The activation energies represent the hopping energy barriers according to the nearest neighbor hopping mechanism, and can also be explained as the depth of shallow traps of charge carriers according to the multiple trapping and releasing mechanism.[30,31] However, the slight superlinearity between conductivity and $1/T$ is noted for $Ni_3(HITT)_2$ when a wider temperature range between 100 and 300 K is considered (Figure 3a), suggesting the presence of multiple activation energies and pointing toward an alternative conduction mechanism at low temperatures. Indeed, fitting the VT data between 100 and 150 K yields a significantly lower activation energy of only 31 meV for $Ni_3(HITT)_2$ (Figure 3a). On the other hand, the VT conductivity data of $Ni_3(HITT)_2$ match

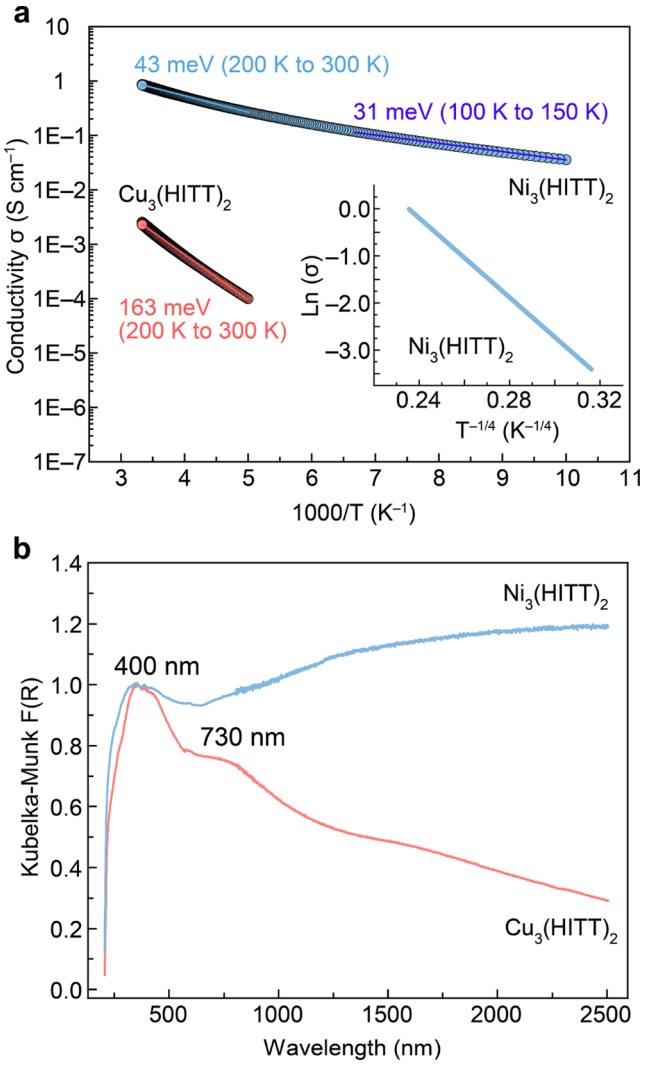

Figure 3. Electrical and optical properties of $Ni_3(HITT)_2$ and $Cu_3(HITT)_2$. (a) Temperature dependence of electrical conductivity, plotted according to the Arrhenius equation. Solid lines represent the best linear fit in corresponding selected temperature ranges. Inset shows the variable-temperature (VT) conductivity data of $Ni_3(HITT)_2$ plotted according to Mott's variable-range hopping (VRH) mechanism. (b) Diffuse reflectance UV–vis–NIR spectra of $Ni_3(HITT)_2$ and $Cu_3(HITT)_2$; data normalized with the ligand centered absorption at 400 nm.

well with the Mott variable-range hopping (VRH) mechanism instead:[32]

$$\sigma_{e,T} = \sigma_{e,0} \exp[-(T_0/T)^{1/d+1}]$$

where d is the dimensionality of carrier transport (d = 3 for $Ni_3(HITT)_2$), $\sigma_{e,0}$ is the temperature-independent constant and equals the value of $\sigma_{e,T}$ when temperature becomes infinite, and T_0 is the material-specific Mott temperature (Figure 3a, inset). Facile charge transport in three dimensions is in a great agreement with the excellent in-plane extended π–d conjugation and out-of-plane π–π stacking of $Ni_3(HITT)_2$.

To understand the origin of substantially higher electrical conductivity in $Ni_3(HITT)_2$ relative to $Cu_3(HITT)_2$, diffuse-reflectance ultraviolet-visible-near IR (DRUV-vis-NIR) spectroscopic characterizations of both materials were conducted under an N_2 atmosphere. The absorption band centered

https://doi.org/10.1021/jacs.4c06935
J. Am. Chem. Soc. 2024, 146, 20500–20507

around 400 nm, observed in the DRUV-vis-NIR spectra of both materials, is characteristic of a ligand-centered electronic transition (Figure 3b). The broad peak centered at 730 nm in the spectrum of $Cu_3(HITT)_2$ is assigned to intervalence charge transfer (IVCT) between Cu^+ and Cu^{2+} centers (Figure 3b), and is characteristic of Class II mixed-valence compounds in the Robin-Day classification.[33] $Ni_3(HITT)_2$ exhibits significantly stronger absorption in the NIR range than $Cu_3(HITT)_2$, suggesting that the degree of in-plane $\pi-d$ electronic delocalization in $Ni_3(HITT)_2$ is significantly higher than that in $Cu_3(HITT)_2$ and is indicative of stronger electronic coupling between Ni^{2+} and HITT ligands. It should be noted that although the contribution from out-of-plane $\pi-\pi$ interactions cannot be ignored, it is probably not the key factor accounting for the difference in electrical conductivity for $Ni_3(HITT)_2$ and $Cu_3(HITT)_2$ since their stacking mode and interlayer distances are nearly identical. Moreover, $Ni_3(HITT)_2$ exhibits uncommonly strong low-energy background absorption, likely stemming from a larger amount of free charge carriers and/or stronger electron−phonon coupling in this frequency region (Figure S30), which itself is responsible for the considerably higher electrical conductivity relative to $Cu_3(HITT)_2$. In fact, we hypothesize that $Ni_3(HITT)_2$ is intrinsically metallic given its broad and metal-like absorption features, but the presence of defects, grain boundaries, and interparticle hopping dominates transport, which appears as thermally activated. This behavior has been observed with other Ni-diamine MOFs[5,23] and is likely best described within the model of granular metals.[34,35]

Indeed, the calculated band structure of $Ni_3(HITT)_2$ reveals the characteristic metallic feature in the out-of-plane direction, as the Fermi level crosses a band in the A-to-Γ direction. A Dirac cone is observed in the in-plane (Γ−M−K−Γ) direction, indicating a semimetal behavior (Figure 4a). Notably, Dirac materials like graphene are known to exhibit exotic physical properties.[36,37] In contrast, although $Cu_3(HITT)_2$ is also calculated to be metallic in the out-of-plane direction, it has a band gap of 0.16 eV in the in-plane direction (Figure 4b). The band dispersion along the in-plane direction for $Cu_3(HITT)_2$ is also notably smaller than that of $Ni_3(HITT)_2$, matching well with the lower electrical conductivity and higher transport activation energy observed in $Cu_3(HITT)_2$. These calculations offer a glimpse into influence exerted by the nature of the metal for in-plane charge transport. Further supporting the experimental observations, density of states (DOS) calculations suggest that Ni contributes significantly to the frontier bands of $Ni_3(HITT)_2$, whereas the contribution from Cu to the frontier bands of $Cu_3(HITT)_2$ is very limited. This result indicates the importance of matching energy levels of metal centers and ligands toward highly conductive 2D cMOFs.

Interestingly, we found that the electrical conductivity of $Cu_3(HITT)_2$ slowly, but substantially decreases from 2.9×10^{-2} to 7.1×10^{-6} S cm^{-1} upon air exposure over the course of 50 days (Figures 5a, S31 and S32). The decrease in conductivity is more rapid early, dropping about 3 orders of magnitude in the first 15 days, to eventually stabilize at approximately 10^{-6} S cm^{-1}, representing an overall modulation of electrical conductivity of nearly 4 orders of magnitude. In contrast, the conductivity of $Ni_3(HITT)_2$ remains essentially unchanged between 4 and 4.5 S cm^{-1} upon air exposure for a similar duration (Figure 5a).

To reveal the origin of this drastic modulation in conductivity, we utilized XPS to investigate the evolution of

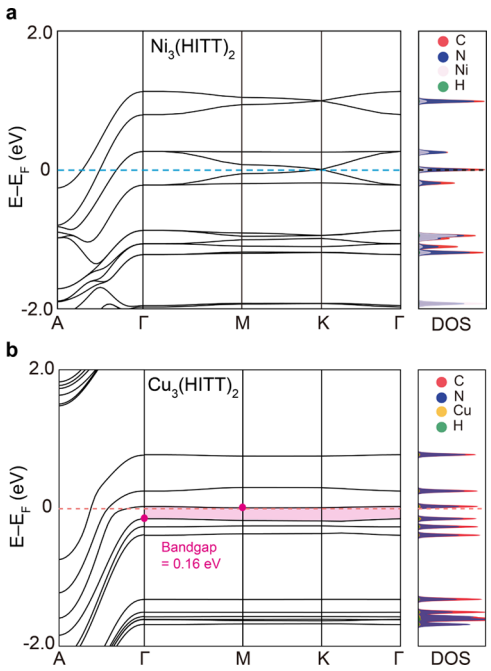

Figure 4. Density functional theory (DFT) calculated electronic band structure and density of states (DOS) of (a) pristine $Ni_3(HITT)_2$ and (b) pristine $Cu_3(HITT)_2$. The blue and pink dotted lines indicate the Fermi level of $Ni_3(HITT)_2$ and $Cu_3(HITT)_2$. The DOS was analyzed at the K point.

metal oxidation states in $M_3(HITT)_2$. As expected, the oxidation state of Ni centers in $Ni_3(HITT)_2$ remained +2 before and after air exposure (Figure S33). However, deconvolution of the Cu $2p_{3/2}$ region in the XPS data clearly revealed gradual oxidation of Cu^+ centers in $Cu_3(HITT)_2$ to Cu^{2+}: the Cu^{2+}/Cu^+ ratio increased as a function of time from 0.66 in the pristine (i.e., Cu^+-rich) state to 7.26 (i.e., Cu^{2+}-rich) after 45 days (Figure 5a,b). The ratio changed only slightly beyond 45 days from 7.26 to 8.25 after 83 days, matching well with the conductivity vales plateauing out over time.

DRUV-vis-NIR spectra of air-exposed $Cu_3(HITT)_2$ recorded at various time intervals spanning 45 days further substantiated our formal oxidation state assignments (Figure 5c). The evolution of the $Cu_3(HITT)_2$ spectra correlates well with the increasing Cu^{2+}/Cu^+ ratio. In particular, the IVCT band corresponding to electron transfer between nearly equimolar Cu^+ and Cu^{2+} centers quickly vanishes upon air exposure due to the continuous increase of the Cu^{2+}/Cu^+ ratio (Figure 5c). A similar phenomenon has been reported in the air exposure study of $Fe_2(BDT)_3$ (BDT = 5,5′(1,4-phenylene)-bis(1*H*-tetrazole)) where an IVCT band gradually increases with formation of Fe^{3+} centers from a formally all-Fe^{2+} parent MOF.[38] Extracting optical gaps (E_0) from the DRUV-vis spectra by plotting the data in the Tauc coordinate reveals that E_0 increases from 1.03 eV for the pristine $Cu_3(HITT)_2$ to 1.29 eV after 45 days of air exposure, matching well with the decrease of electrical conductivity (Figures 5d and S34).

Density functional theory (DFT) calculations provided insight into the observed decrease in electrical conductivity upon exposure to air (Figures S35−S37). We modeled the air exposed $Cu_3(HITT)_2$ by removing a single electron to make a partially oxidized system. Oxidation expectedly decreases electron occupancy in the valence band (VB) and lowers the Fermi energy. However, removal of one electron also notably

https://doi.org/10.1021/jacs.4c06935
J. Am. Chem. Soc. 2024, 146, 20500−20507

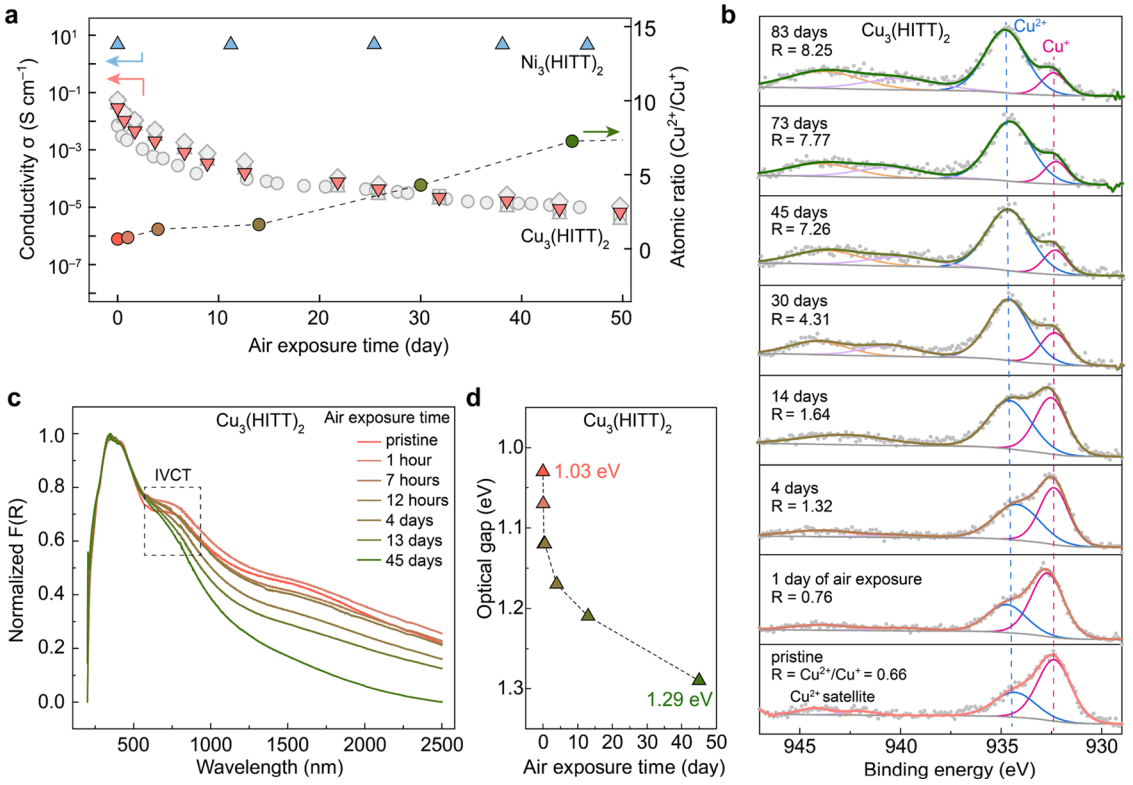

Figure 5. Characterization of $Cu_3(HITT)_2$ exposed to ambient atmosphere for different durations. (a) The evolution of electrical conductivity of $Ni_3(HITT)_2$ and $Cu_3(HITT)_2$ and the corresponding atomic Cu^{2+}/Cu^{+} ratio upon air exposure. Gray scatters represent four individual devices of $Cu_3(HITT)_2$ and pink triangles represent the average values. (b) Fitting of high-resolution Cu 2p XPS data for oxidation state analysis. (c) Diffuse reflectance UV−vis−NIR spectra and (d) corresponding optical gap obtained from Tauc plots.

increases the bandgap from 0.16 to 1.0 eV in the in-plane direction (blue region in Figure S35). It further affects the dispersion widths of the VB and conduction band (CB), which decrease from 35.32 and 19.62 meV, respectively, in pristine $Cu_3(HITT)_2$, to only 1.43 and 2.23 meV, respectively, after oxidation. The narrowing of the bandwidth would lead to an unexpected reduction for the in-plane charge mobility upon oxidation. The increased bandgap and diminished band dispersion align well with the reduction in conductivity and the evolution of the DRUV-vis-NIR spectra following air exposure.

CONCLUSIONS

Overall, the results presented here solidify the superiority of nickel-amino/imino-bridged materials among 2D cMOFs with respect to charge transport: with a conductivity of 4.5 S cm^{-1}, $Ni_3(HITT)_2$ allows for significantly better transport than its Cu analog and is among the most conductive MOFs to date. Spectroscopic analysis and calculations indicate that Ni^{2+} centers exhibit stronger electronic interaction with HITT ligands, resulting in significantly enhanced $\pi-d$ conjugation, and contribute significantly more to the DOS of frontier bands in comparison with Cu centers. We assign these facts as at least partially responsible for the 2 orders of magnitude higher electrical conductivity compared to $Cu_3(HITT)_2$. In addition, we find that the Cu^{2+}/Cu^{+} ratio also significantly affects the electrical conductivity of $Cu_3(HITT)_2$. These results encourage further fundamental studies of structure- and composition-property relationships of 2D cMOFs and provide deeper understanding of the influence of metal nodes on the conductivity of cMOFs.

ASSOCIATED CONTENT

Supporting Information

The Supporting Information is available free of charge at https://pubs.acs.org/doi/10.1021/jacs.4c06935.

Materials and methods, experimental procedures for synthesis and characterization data of ligands and MOFs (PDF)

AUTHOR INFORMATION

Corresponding Author

Mircea Dincă − *Department of Chemistry, Massachusetts Institute of Technology, Cambridge, Massachusetts 02139, United States;* orcid.org/0000-0002-1262-1264; Email: mdinca@mit.edu

Authors

Jiande Wang − *Department of Chemistry, Massachusetts Institute of Technology, Cambridge, Massachusetts 02139, United States*

Tianyang Chen − *Department of Chemistry, Massachusetts Institute of Technology, Cambridge, Massachusetts 02139, United States;* orcid.org/0000-0003-3142-8176

Mingyu Jeon − *Department of Chemistry, Massachusetts Institute of Technology, Cambridge, Massachusetts 02139, United States; Department of Chemical and Biomolecular Engineering, Korea Advanced Institute of Science and Technology (KAIST), Daejeon 34141, Republic of Korea;* orcid.org/0000-0002-8285-5197

Julius J. Oppenheim − *Department of Chemistry, Massachusetts Institute of Technology, Cambridge,*

https://doi.org/10.1021/jacs.4c06935
J. Am. Chem. Soc. 2024, 146, 20500−20507

Massachusetts 02139, United States; orcid.org/0000-0002-5988-0677

Bowen Tan − *Department of Chemistry, Massachusetts Institute of Technology, Cambridge, Massachusetts 02139, United States;* orcid.org/0000-0002-5166-1541

Jihan Kim − *Department of Chemical and Biomolecular Engineering, Korea Advanced Institute of Science and Technology (KAIST), Daejeon 34141, Republic of Korea;* orcid.org/0000-0002-3844-8789

Complete contact information is available at: https://pubs.acs.org/10.1021/jacs.4c06935

Author Contributions

[§]J.W. and T.C. contributed equally to this work. All authors have given approval to the final version of the manuscript.

Notes

The authors declare no competing financial interest.

■ ACKNOWLEDGMENTS

This work was supported by Department of Energy, Basic Energy Sciences, through award DE-SC0023288 to M.D. M.J. and J.K. acknowledge the National Nanofab Center (N02240024) in South Korea. Cryo-EM specimens were prepared and imaged at the Automated Cryogenic Electron Microscopy Facility in MIT.nano on a Talos Arctica microscope, a gift from the Arnold and Mabel Beckman Foundation.

■ REFERENCES

(1) Xie, L. S.; Skorupskii, G.; Dincă, M. Electrically Conductive Metal−Organic Frameworks. *Chem. Rev.* **2020**, *120*, 8536−8580.

(2) Sun, L.; Campbell, M. G.; Dincă, M. Electrically Conductive Porous Metal-Organic Frameworks. *Angew. Chem., Int. Ed.* **2016**, *55*, 3566−79.

(3) Day, R. W.; Bediako, D. K.; Rezaee, M.; Parent, L. R.; Skorupskii, G.; Arguilla, M. Q.; Hendon, C. H.; Stassen, I.; Gianneschi, N. C.; Kim, P.; Dincă, M. Single Crystals of Electrically Conductive Two-Dimensional Metal-Organic Frameworks: Structural and Electrical Transport Properties. *ACS Cent. Sci.* **2019**, *5*, 1959−1964.

(4) Skorupskii, G.; Le, K. N.; Cordova, D. L. M.; Yang, L.; Chen, T.; Hendon, C. H.; Arguilla, M. Q.; Dincă, M. Porous lanthanide metal-organic frameworks with metallic conductivity. *Proc. Natl. Acad. Sci. U.S.A.* **2022**, *119*, No. e2205127119.

(5) Dou, J.-H.; Sun, L.; Ge, Y.; Li, W.; Hendon, C. H.; Li, J.; Gul, S.; Yano, J.; Stach, E. A.; Dincă, M. Signature of Metallic Behavior in the Metal−Organic Frameworks M_3(hexaiminobenzene)$_2$ (M = Ni, Cu). *J. Am. Chem. Soc.* **2017**, *139*, 13608−13611.

(6) Huang, X.; Zhang, S.; Liu, L.; Yu, L.; Chen, G.; Xu, W.; Zhu, D. Superconductivity in a Copper(II)-Based Coordination Polymer with Perfect Kagome Structure. *Angew. Chem., Int. Ed.* **2018**, *57*, 146−150.

(7) Zhong, H.; Wang, M.; Chen, G.; Dong, R.; Feng, X. Two-Dimensional Conjugated Metal−Organic Frameworks for Electrocatalysis: Opportunities and Challenges. *ACS Nano* **2022**, *16*, 1759−1780.

(8) Mariano, R. G.; Wahab, O. J.; Rabinowitz, J. A.; Oppenheim, J.; Chen, T.; Unwin, P. R.; Dincă, M. Thousand-fold increase in O_2 electroreduction rates with conductive MOFs. *ACS Cent. Sci.* **2022**, *8*, 975−982.

(9) Wu, G.; Huang, J.; Zang, Y.; He, J.; Xu, G. Porous Field-Effect Transistors Based on a Semiconductive Metal−Organic Framework. *J. Am. Chem. Soc.* **2017**, *139*, 1360−1363.

(10) Koo, W.-T.; Jang, J.-S.; Kim, I.-D. Metal-Organic Frameworks for Chemiresistive Sensors. *Chem* **2019**, *5*, 1938−1963.

(11) Stassen, I.; Dou, J. H.; Hendon, C.; Dincă, M. Chemiresistive Sensing of Ambient CO_2 by an Autogenously Hydrated Cu_3(hexaiminobenzene)$_2$ Framework. *ACS Cent. Sci.* **2019**, *5*, 1425−1431.

(12) Campbell, M. G.; Sheberla, D.; Liu, S. F.; Swager, T. M.; Dincă, M. Cu_3(hexaiminotriphenylene)$_2$: an electrically conductive 2D metal-organic framework for chemiresistive sensing. *Angew. Chem., Int. Ed.* **2015**, *54*, 4349−52.

(13) Campbell, M. G.; Liu, S. F.; Swager, T. M.; Dincă, M. Chemiresistive Sensor Arrays from Conductive 2D Metal-Organic Frameworks. *J. Am. Chem. Soc.* **2015**, *137*, 13780−3.

(14) Aykanat, A.; Meng, Z.; Stolz, R. M.; Morrell, C. T.; Mirica, K. A. Bimetallic Two-Dimensional Metal-Organic Frameworks for the Chemiresistive Detection of Carbon Monoxide. *Angew. Chem., Int. Ed.* **2022**, *61*, No. e202113665.

(15) Niu, L.; Wu, T.; Chen, M.; Yang, L.; Yang, J.; Wang, Z.; Kornyshev, A. A.; Jiang, H.; Bi, S.; Feng, G. Conductive Metal−Organic Frameworks for Supercapacitors. *Adv. Mater.* **2022**, *34*, No. 2200999.

(16) Sheberla, D.; Bachman, J. C.; Elias, J. S.; Sun, C.-J.; Shao-Horn, Y.; Dincă, M. Conductive MOF electrodes for stable supercapacitors with high areal capacitance. *Nat. Mater.* **2017**, *16*, 220−224.

(17) Bi, S.; Banda, H.; Chen, M.; Niu, L.; Chen, M.; Wu, T.; Wang, J.; Wang, R.; Feng, J.; Chen, T.; Dincă, M.; Kornyshev, A. A.; Feng, G. Molecular understanding of charge storage and charging dynamics in supercapacitors with MOF electrodes and ionic liquid electrolytes. *Nat. Mater.* **2020**, *19*, 552−558.

(18) Feng, D.; Lei, T.; Lukatskaya, M. R.; Park, J.; Huang, Z.; Lee, M.; Shaw, L.; Chen, S.; Yakovenko, A. A.; Kulkarni, A.; Xiao, J.; Fredrickson, K.; Tok, J. B.; Zou, X.; Cui, Y.; Bao, Z. Robust and conductive two-dimensional metal−organic frameworks with exceptionally high volumetric and areal capacitance. *Nat. Energy* **2018**, *3*, 30−36.

(19) Zhang, Y.; Wang, J.; Apostol, P.; Rambabu, D.; Eddine Lakraychi, A.; Guo, X.; Zhang, X.; Lin, X.; Pal, S.; Rao Bakuru, V.; Chen, X.; Vlad, A. Bimetallic Anionic Organic Frameworks with Solid-State Cation Conduction for Charge Storage Applications. *Angew. Chem., Int. Ed.* **2023**, *62*, No. e202310033.

(20) Rambabu, D.; Lakraychi, A. E.; Wang, J.; Sieuw, L.; Gupta, D.; Apostol, P.; Chanteux, G.; Goossens, T.; Robeyns, K.; Vlad, A. An Electrically Conducting Li-Ion Metal−Organic Framework. *J. Am. Chem. Soc.* **2021**, *143*, 11641−11650.

(21) Sun, L.; Yang, L.; Dou, J. H.; Li, J.; Skorupskii, G.; Mardini, M.; Tan, K. O.; Chen, T.; Sun, C.; Oppenheim, J. J.; Griffin, R. G.; Dincă, M.; Rajh, T. Room-Temperature Quantitative Quantum Sensing of Lithium Ions with a Radical-Embedded Metal-Organic Framework. *J. Am. Chem. Soc.* **2022**, *144*, 19008−19016.

(22) Chen, T.; Dou, J. H.; Yang, L.; Sun, C.; Libretto, N. J.; Skorupskii, G.; Miller, J. T.; Dincă, M. Continuous Electrical Conductivity Variation in M_3(Hexaiminotriphenylene)$_2$ (M = Co, Ni, Cu) MOF Alloys. *J. Am. Chem. Soc.* **2020**, *142*, 12367−12373.

(23) Sheberla, D.; Sun, L.; Blood-Forsythe, M. A.; Er, S.; Wade, C. R.; Brozek, C. K.; Aspuru-Guzik, A.; Dincă, M. High Electrical Conductivity in Ni_3(2,3,6,7,10,11-hexaiminotriphenylene)$_2$, a Semiconducting Metal−Organic Graphene Analogue. *J. Am. Chem. Soc.* **2014**, *136*, 8859−8862.

(24) Lahiri, N.; Lotfizadeh, N.; Tsuchikawa, R.; Deshpande, V. V.; Louie, J. Hexaaminobenzene as a building block for a Family of 2D Coordination Polymers. *J. Am. Chem. Soc.* **2017**, *139*, 19−22.

(25) Zhang, P.; Wang, M.; Liu, Y.; Yang, S.; Wang, F.; Li, Y.; Chen, G.; Li, Z.; Wang, G.; Zhu, M.; Dong, R.; Yu, M.; Schmidt, O. G.; Feng, X. Dual-Redox-Sites Enable Two-Dimensional Conjugated Metal-Organic Frameworks with Large Pseudocapacitance and Wide Potential Window. *J. Am. Chem. Soc.* **2021**, *143*, 10168−10176.

(26) Apostol, P.; Gali, S. M.; Su, A.; Tie, D.; Zhang, Y.; Pal, S.; Lin, X.; Bakuru, V. R.; Rambabu, D.; Beljonne, D.; Dincă, M.; Vlad, A. Controlling Charge Transport in 2D Conductive MOFs horizontal lin—The Role of Nitrogen-Rich Ligands and Chemical Functionality. *J. Am. Chem. Soc.* **2023**, *145*, 24669−24677.

(27) Lu, Y.; Zhang, Y.; Yang, C.-Y.; Revuelta, S.; Qi, H.; Huang, C.; Jin, W.; Li, Z.; Vega-Mayoral, V.; Liu, Y.; Huang, X.; Pohl, D.; Položij, M.; Zhou, S.; Cánovas, E.; Heine, T.; Fabiano, S.; Feng, X.; Dong, R. Precise tuning of interlayer electronic coupling in layered conductive metal-organic frameworks. *Nat. Commun.* **2022**, *13*, No. 7240.
(28) Dou, J. H.; Arguilla, M. Q.; Luo, Y.; Li, J.; Zhang, W.; Sun, L.; Mancuso, J. L.; Yang, L.; Chen, T.; Parent, L. R.; Skorupskii, G.; Libretto, N. J.; Sun, C.; Yang, M. C.; Dip, P. V.; Brignole, E. J.; Miller, J. T.; Kong, J.; Hendon, C. H.; Sun, J.; Dincă, M. Atomically precise single-crystal structures of electrically conducting 2D metal-organic frameworks. *Nat. Mater.* **2021**, *20*, 222−228.
(29) Barrett, E. P.; Joyner, L. G.; Halenda, P. P. The Determination of Pore Volume and Area Distributions in Porous Substances. I. Computations from Nitrogen Isotherms. *J. Am. Chem. Soc.* **1951**, *73*, 373−380.
(30) Mott, N. F. Electrons in disordered structures. *Adv. Phys.* **1967**, *16*, 49−144.
(31) Gantmakher, V. F. 58 Hopping Conductivity. In *Electrons and Disorder in Solids*; Gantmakher, V. F., Ed.; Oxford University Press, 2005.
(32) Mott, N. F. Conduction in glasses containing transition metal ions. *J. Non-Cryst. Solids* **1968**, *1*, 1−17.
(33) Robin, M. B.; Day, P. Mixed Valence Chemistry-A Survey and Classification. In *Advances in Inorganic Chemistry and Radiochemistry*; Emeléus, H. J.; Sharpe, A. G., Eds.; Academic Press, 1968; Vol. *10*, pp 247−422.
(34) Staller, C. M.; Robinson, Z. L.; Agrawal, A.; Gibbs, S. L.; Greenberg, B. L.; Lounis, S. D.; Kortshagen, U. R.; Milliron, D. J. Tuning Nanocrystal Surface Depletion by Controlling Dopant Distribution as a Route Toward Enhanced Film Conductivity. *Nano Lett.* **2018**, *18*, 2870−2878.
(35) Staller, C. M.; Gibbs, S. L.; Gan, X. Y.; Bender, J. T.; Jarvis, K.; Ong, G. K.; Milliron, D. J. Contact Conductance Governs Metallicity in Conducting Metal Oxide Nanocrystal Films. *Nano Lett.* **2022**, *22*, 5009−5014.
(36) Novoselov, K. S.; Geim, A. K.; Morozov, S. V.; Jiang, D.; Katsnelson, M. I.; Grigorieva, I. V.; Dubonos, S. V.; Firsov, A. A. Two-dimensional gas of massless Dirac fermions in graphene. *Nature* **2005**, *438*, 197−200.
(37) Zhang, Y.; Tan, Y.-W.; Stormer, H. L.; Kim, P. Experimental observation of the quantum Hall effect and Berry's phase in graphene. *Nature* **2005**, *438*, 201−204.
(38) Xie, L. S.; Sun, L.; Wan, R.; Park, S. S.; DeGayner, J. A.; Hendon, C. H.; Dincă, M. Tunable Mixed-Valence Doping toward Record Electrical Conductivity in a Three-Dimensional Metal−Organic Framework. *J. Am. Chem. Soc.* **2018**, *140*, 7411−7414.

https://doi.org/10.1021/jacs.4c06935
J. Am. Chem. Soc. 2024, 146, 20500−20507